nature communications

Article

https://doi.org/10.1038/s41467-026-69353-9

Mechanochemical engineering of chiroptical properties in indium-based chiral metal halides by grinding

Received: 21 September 2025

Accepted: 28 January 2026

Published online: 11 February 2026

Check for updates

Junhong Wu, Hao Li, Jialu Wang, Xiaorui Yang, Tianyong Zhang, Bin Li & Shuang Jiang

Circularly polarized luminescence is crucial for optoelectronics, bioimaging, and three-dimensional display, yet most of current materials suffer from complex synthesis and limited tunability. Herein, we show the regulation of chiroptical properties in metal halides through mechanochemical engineering. Specifically, phosphorescent indium-based chiral metal halides exhibit blue circularly polarized luminescence, along with antimony-doped indium-based metal halides emit orange circularly polarized luminescence. A grinding strategy using bromide salts like potassium bromide induces bright yellow fluorescence and enables versatile circularly polarized luminescence modulation. When antimony-doped indium-based metal halides are ground with five different bromide salts, it exhibits intriguing and tunable properties: (i) enhanced circularly polarized luminescence, with a luminescence dissymmetry factor value up to 10^{-2}; (ii) inversion of the circularly polarized luminescence signal; (iii) generation of near-infrared circularly polarized luminescence with a substantial Stokes shift of 370 nm; and most notably, (iv) a 29.71-fold improvement in second-harmonic generation efficiency. This approach also realizes applications in circularly polarized light-emitting diodes.

Materials with circularly polarized luminescence (CPL) activity have attracted extensive attention due to their potential applications in various fields such as three-dimensional (3D) optical displays[1], storage devices[2,3], molecular switches[4,5], optical sensors[6–8], information storage[9–11], and chiral sensing[12]. The high-performance CPL materials require bright photoluminescence (PL), high photoluminescence quantum yield (PLQY) and a large luminescence dissymmetry factor (g_{lum})[13]. Theoretically, achieving a high g_{lum} depends on the balanced contribution of the magnetic transition dipole moment and the electric transition dipole moment, in terms of both their magnitude and relative orientation[14]. However, due to the intrinsic mismatch between magnetic and electric dipole transitions, simultaneously achieving high PLQY and g_{lum} remains a challenge. Chiral organic-inorganic metal halides have emerged as promising candidates for CPL materials owing to their tunable optoelectronic properties[15–18].

Current CPL regulation of chiral metal halides can be categorized into two approaches: crystal synthesis and post-regulation by external stimulation[19]. The former approach predominantly relies on the selection of organic ligands and strategic metal doping during crystal growth[20]. For instance, to obtain near-infrared (NIR) CPL, it is necessary to select the introduction of rare earth metals or iodide ions during the synthesis of the crystal[21,22]. However, the growth of single crystals often requires a considerable time investment, and the quality of the crystals must be carefully monitored to obtain high-performance CPL metal halide materials[23,24]. Recent studies have demonstrated post-synthetic CPL modulation through external stimuli, such as solvent treatment (e.g., dimethylformamide or acetonitrile)[25,26], or high-pressure treatment[27]. These approaches have laid the foundation for obtaining multi-colored, high-g_{lum} (>10^{-3}) chiral metal halides. However, the current post-regulation methods for the CPL of metal halides are

School of Chemical Engineering and Technology, Tianjin University, Tianjin, P. R. China. e-mail: shuangjiang@tju.edu.cn

https://doi.org/10.1038/s41467-026-69353-9

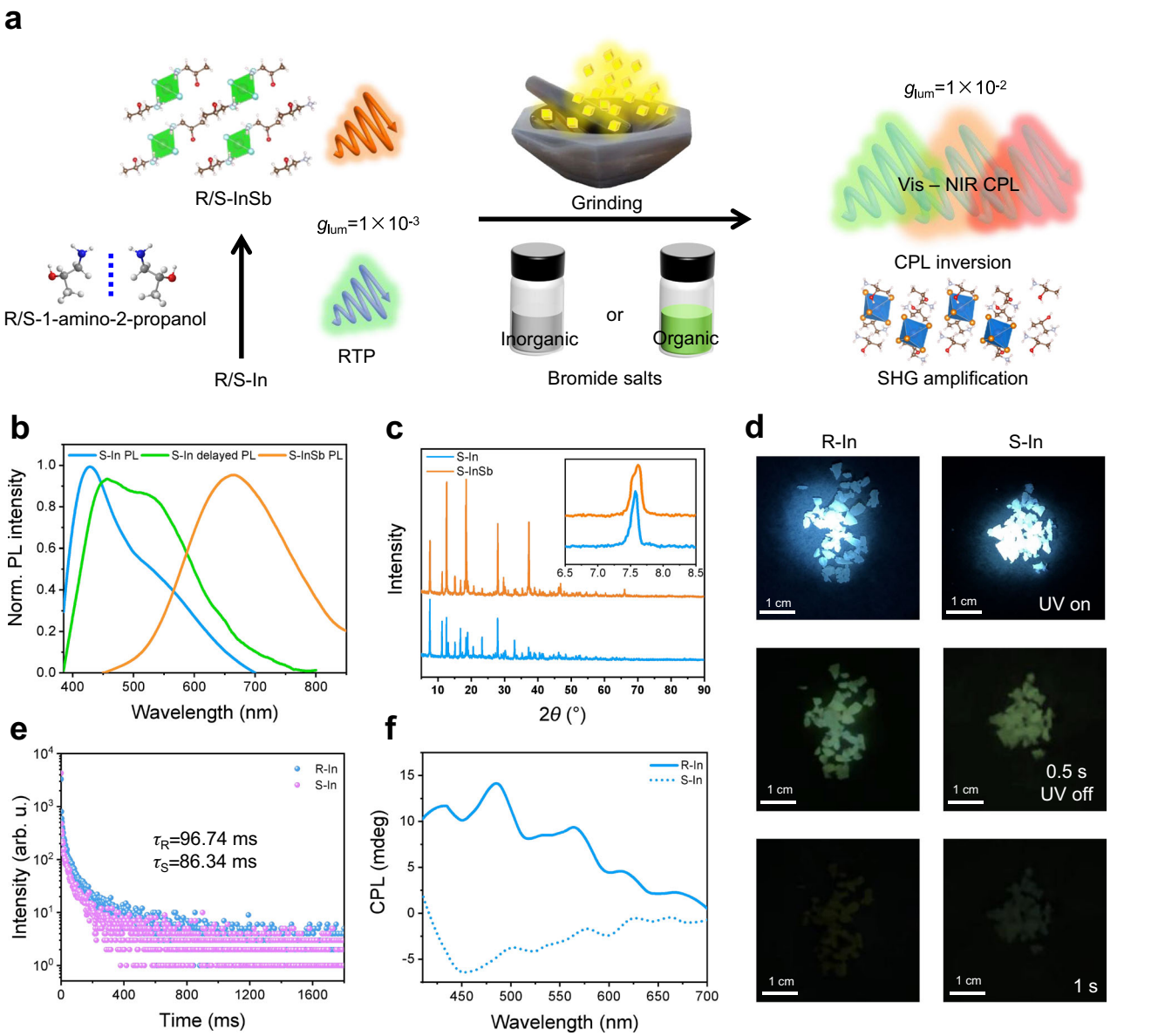

Fig. 1 | Schematic diagram of the grinding strategy for enhancing chiral optical properties and the photophysical properties of R/S-In and R/S-InSb crystals. **a** Schematic diagram of the grinding strategy for boosting chiral optical properties. **b** PL and delay PL spectra of S-In and S-InSb crystals. **c** PXRD patterns of S-In (blue line) and S-InSb (orange line). **d** PL and RTP behaviors of R/S-In. **e** Time-resolved PL decay curves of R/S-In. **f** The CPL spectra of R/S-In. Source data are provided as a Source Data file.

relatively limited with strict experimental conditions and complex synthetic processes, featuring high time costs and restricted CPL signal regulation[28–31]. Therefore, it is urgent and necessary to develop simple and versatile ways to achieve effective and universal regulation of CPL properties for chiral metal halide materials[32].

In this work, we have developed a simple, rapid and generally applicable grinding strategy for post-regulation of chiral perovskites. First, chiral indium metal halides R/S-(1-amino-2-propanol)$_2$InCl$_5$ (denoted as R/S-In) were constructed through appropriate chiral selection ((R)-(-)-1-amino-2-propanol, (S)-(+)-1-amino-2-propanol), which show room-temperature phosphorescence (RTP) with long luminescence lifetimes of 96.74 and 86.34 ms, along with blue CPL emission. With the doping of Sb, R/S-InSb were obtained, which show orange symmetric CPL signals. Grinding R/S-InSb with a series of bromide salts enables tuning of the chiroptical and nonlinear optical properties. Both inorganic and organic salts can enhance the luminescence performance through grinding, thereby amplifying $|g_{lum}|$ to the 10^{-2} level. The selection of salts can also modulate the PL emission wavelength. After grinding R/S-InSb with FABr, the CPL signal in the visible light region red-shifts to the NIR region without adding any rare earth metals or introducing iodide ions. In addition to achieving multi-color CPL regulation, the grinding strategy can also reverse the CPL signal and enhance the second-harmonic generation (SHG) signal by 29.71-fold (Fig. 1a). Meanwhile, the grinding strategy endows the material with adjustable chiral optical properties, affording application potential in circularly polarized light-emitting diodes (CP-LEDs). In summary, this simple post-regulation strategy provides an approach for the preparation and application of high-performance chiral metal halides.

Results

Optical properties of chiral indium-based metal halide

The chiral indium-based metal halides R/S-In were synthesized via a hydrothermal method using chiral amino alcohol ligands ((R)-(-)-1-amino-2-propanol and (S)-(+)-1-amino-2-propanol). The phase purity and structural integrity were verified by powder X-ray diffraction

https://doi.org/10.1038/s41467-026-69353-9

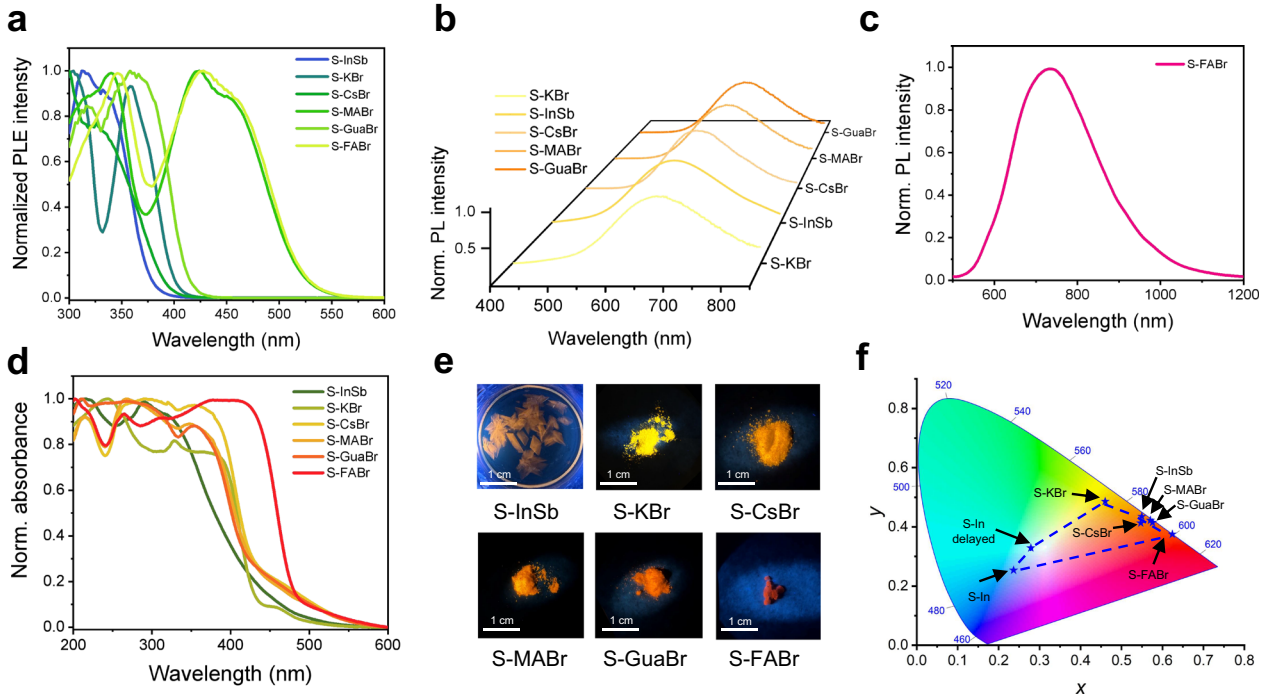

Fig. 2 | The optical physical properties of the ground sample. a The PLE spectra of S-InSb, S-KBr, S-CsBr, S-MABr, S-GuaBr and S-FABr. **b** The PL spectra of S-InSb, S-KBr, S-CsBr, S-MABr, S-GuaBr and (**c**) S-FABr. **d** The absorbance spectra of S-InSb, S-KBr, S-CsBr, S-MABr, S-GuaBr and S-FABr. **e** PL photos of the S-InSb and the samples after grinding treatment under 365 nm ultraviolet light irradiation. **f** The CIE of S-In, S-InSb, S-KBr, S-CsBr, S-MABr, S-GuaBr and S-FABr. Source data are provided as a Source data file.

(PXRD) analysis (Supplementary Fig. 1). Steady-state PL spectra reveal a primary emission band centered at 440 nm with a broad spectral profile spanning the 400-700 nm range, corresponding to sky-blue PL under UV excitation. Notably, persistent phosphorescence was directly observed in R/S-In samples after the cessation of UV irradiation. The phosphorescent nature of the emission was further verified by delayed PL spectra and time-resolved PL decay curves (Fig. 1b–e). The phosphorescence lifetime of R-In was tested as 96.74 ms, and that of S-In was tested as 86.34 ms[33,34]. Further, the chiral optical properties of R/S-In were studied. As shown in Supplementary Fig. 2, there is a symmetrical circular dichroism (CD) signal in the 300-450 nm region of R/S-In, indicating that the chiral ligands have transferred chirality between the In-Cl octahedral structures. Additionally, in the 400-700 nm range, R-In shows a positive CPL signal, while S-In shows a negative CPL signal (Fig. 1f).

Element doping is an effective way to regulate the PL performance of metal halide[35–39]. We introduced 15% Sb into R/S-In to red-shift the PL emission region of metal halides from blue to orange. The emission peak is located at 660 nm, presenting a wide and red-shifted emission peak, indicating that it belongs to the self-trapped state (STE) emission (Fig. 1b)[40–44]. The chiroptical properties of R/S-InSb were tested. The CD spectra revealed distinct mirror-image signals at 415 and 360 nm (Supplementary Fig. 4), indicating that the doping of Sb ions did not cause the disappearance of a chiral structure. As shown in Fig.1c, the main diffraction peak of S-In and S-InSb is at 7.5°, which slightly shifts to a low angle with the doping of Sb^{3+}, indicating that the doping of Sb^{3+} causes a slight lattice expansion, but it does not destroy the In-based crystal structure, and Sb^{3+} cations play a role by replacing In^{3+} cations into the crystal to form PL centers.

Modulation of PL by grinding

Grinding the sample with potassium bromide (KBr) and then pressing it into particles is a common sample preparation method, which is used to characterize its optical properties, including FTIR, UV-Vis, CD, CPL, PL, etc[45–48]. Intriguingly, during our standard preparation of R/S-InSb with KBr, we discovered that the grinding process induced a dramatic color change of the photoluminescence to golden yellow (Supplementary Movie 1). In addition to KBr, various bromide salts including cesium bromide (CsBr), methylammonium bromide (MABr), guanidinium bromide (GuaBr), and formamidinium bromide (FABr) were found to react with R/S-InSb through mechanochemical grinding, yielding a series of composites (R/S-KBr, R/S-CsBr, R/S-MABr, R/S-GuaBr, and R/S-FABr). This outcome underscores the remarkable generality of the grinding strategy for post-synthetic modification. Real-time photographic imaging of the ground crystals reveals emission wavelength shifts, prompting systematic photophysical characterization of the ground samples (Fig. 2a–f). Notably, S-KBr exhibits a 50 nm blue-shift relative to pristine S-InSb, with a dominant emission peak at 600 nm corresponding to bright yellow PL. The PLQY shows a 3.5-fold enhancement, reaching 35.51%. resulted in a red shift of PL spectra of obtained R/S-CsBr, R/S-MABr, R/S-GuaBr and R/S-FABr. In contrast to KBr, grinding R/S-InSb with the other four bromide salts resulted in a distinct red shift in the PL spectra of the resulting composites (R/S-CsBr, R/S-MABr, R/S-GuaBr, and R/S-FABr). It is worth noting that, the emission peak position of S-FABr red shifts to 735 nm, with the Stokes shift as large as 370 nm (Fig.2c). The emission peak extends from 550 to 1200 nm, achieving a wide spectral coverage in the NIR region. Generally speaking, to achieve NIR emission from metal halides, rare earth metal ions need to be introduced or halide ions need to be replaced with I^- anions[49,50]. Remarkably, the metal halides in this work realize NIR emission via a straightforward grinding strategy, without incorporating any rare-earth metals or additional foreign elements. As shown in Fig. 2d, the absorption of the crystals after grinding shifted towards the red compared to the crystals before grinding, which indicates that the Br^- ions have been incorporated into the system. To further investigate the existence form of Br^- in the system, we conducted energy dispersive spectroscopy (EDS) mapping on the ground sample after grinding (Supplementary Fig. 5). The EDS

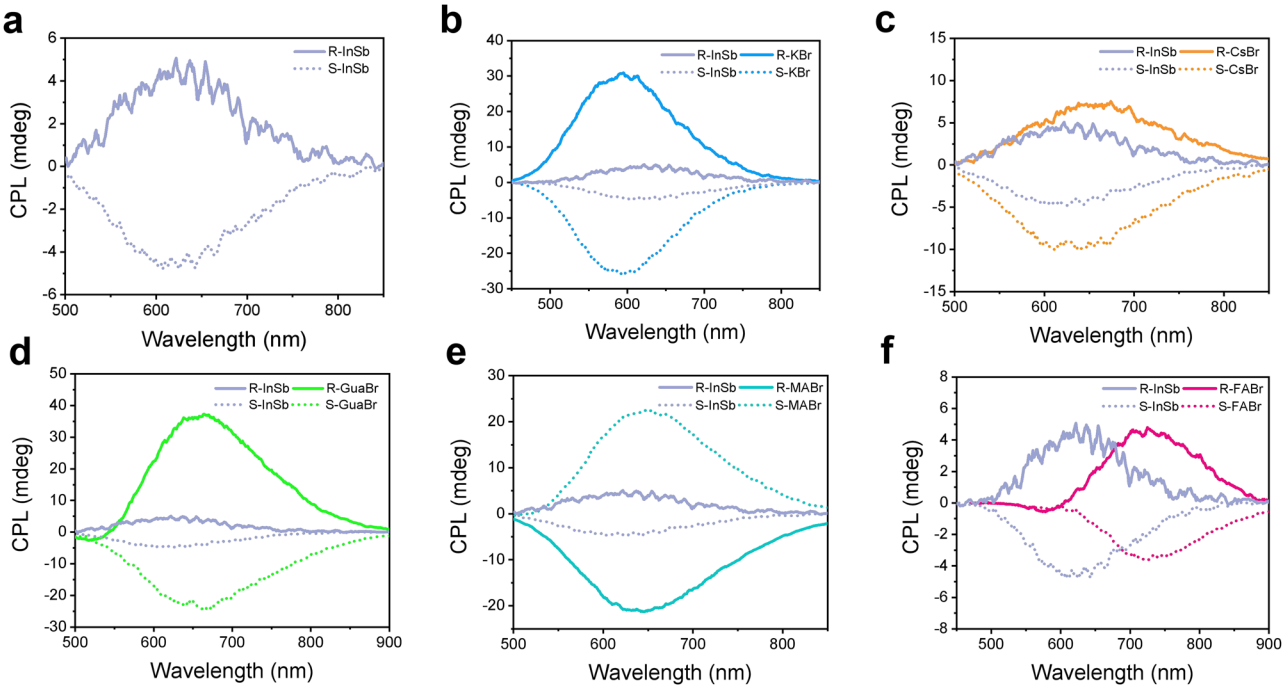

Fig. 3 | CPL properties of grinding samples. The CPL spectra of (**a**) R/S-InSb, (**b**) R/S-KBr, (**c**) R/S-CsBr, (**d**) R/S-GuaBr, (**e**) R/S-MABr and (**f**) R/S-FABr. Source data are provided as a Source data file.

mapping results revealed the overlap between the Br^- and Cl^- signals in the transmission electron microscopy images, indicating a highly homogeneous distribution of Br elements throughout the observed regions, closely coinciding with the Cl distribution. This provides evidence that Br^- has been uniformly doped into the bulk phase of the material. Quantitative analysis of the Br signal relative to the total halogen signal (Br^- + Cl^-) further indicated an influence of the cation species on the bromine substitution process. Specifically, inorganic bromide salts generally resulted in a lower relative atomic percentage of Br compared to organic bromide salts. Notably, the S-KBr sample exhibited the lowest Br relative percentage of merely 12.72%. In contrast, among the organic bromide salts, the S-MABr sample achieved the highest Br relative atomic percentage of 93.48%. To further elucidate the existence form of Br^-, X-ray photoelectron spectroscopy (XPS) analysis was conducted on all ground samples (Supplementary Figs. 6–10). The relative atomic percentages of Br obtained from XPS showed a trend similar to that derived from EDS analysis (Supplementary Table 7). A notable discrepancy was observed for the S-KBr sample, where the Br percentage differed between EDS (bulk-sensitive) and XPS (surface-sensitive) measurements. This suggests a lower efficiency of bromine substitution in S-KBr, with Br^- predominantly located near the sample surface. Conversely, for the S-CsBr, S-MABr, S-FABr, and S-GuaBr samples, the consistent Br percentages from both XPS and EDS mapping indicate a more substantial incorporation of Br^- into the bulk phase.

To thoroughly investigate the universality of our grinding strategy and elucidate the critical role of halide anions, we extended our research to include chloride and iodide salt systems. As shown in Supplementary Fig. 11, the choice of halide anion proved decisive for the optical modulation outcome: most chloride salts (e.g., KCl, CsCl, MACl, GuaCl) induced a blue shift in the photoluminescence spectrum. Although both formamidinium chloride (FACl) and FABr caused a red shift, the magnitude of the shift induced by FABr was greater than that by FACl. Most notably, all iodide salts led to complete fluorescence quenching. These results reveal a synergistic cation-anion mechanism during the grinding process: the nature of the cation primarily governs the direction of the spectral shift, while the properties of the halide anion (particularly its ionic size) dictate the extent and ultimate success of the spectral modulation. This underscores that careful consideration of the size compatibility between the cationic and anionic constituents of the grinding salt is crucial for achieving efficient optical modulation.

Amplification and inversion of CPL by grinding

To investigate the grinding-induced changes in chiral optical properties, we systematically characterized the CD spectra and powder X-ray diffraction (PXRD) patterns of ground samples. Although modified substances were generated after the mechanical chemical treatment, they still maintained the chiral properties and crystal characteristics (Supplementary Figs. 12–22). Corresponding circularly polarized luminescence (CPL) measurements revealed mirror-symmetric signals for the parent R/S-InSb within the 500–800 nm range (Fig. 3a), with R-InSb exhibiting a positive signal and S-InSb showing a negative signal. The g_{lum} value calculated from the CPL signals is approximately $\pm 1 \times 10^{-3}$[51]. We further evaluated the CPL properties of the ground composites—R/S-KBr, R/S-CsBr, R/S-MABr, R/S-GuaBr, and R/S-FABr—as summarized in Fig. 3b–f. Notably, R/S-KBr exhibited a 6-fold enhancement in CPL signal intensity compared to pristine R/S-InSb, with maximum $|g_{lum}|$ values reaching 1×10^{-2} (Supplementary Fig. 24). This indicates that KBr grinding amplifies the CPL dissymmetry factor by an order of magnitude to the 10^{-2} level. This may be due to the fact that the inorganic cation K^+ salt and anion Br^- greatly improves its emission performance, as confirmed by the PLQY characterization (Supplementary Table 8). The PLQY of S-InSb before grinding was 10.46%, and that of S-KBr was ≈3.5 times (35.51%) higher than before grinding. Similarly, S-CsBr also increased the PLQY by a factor of 2 (20.13%), resulting in an increase in the $|g_{lum}|$ to 4×10^{-3} (Supplementary Fig. 25).

Mechanochemical grinding of R/S-InSb with organic salts also enabled CPL signal amplification, demonstrating the general applicability of this strategy. The introduction of FABr caused the main emission peak position to shift from 660 to 735 nm. The CPL spectrum shows a corresponding trend, presenting NIR CPL emission. R-FABr shows a positive signal CPL in the 500–900 nm region, while S-FABr

https://doi.org/10.1038/s41467-026-69353-9

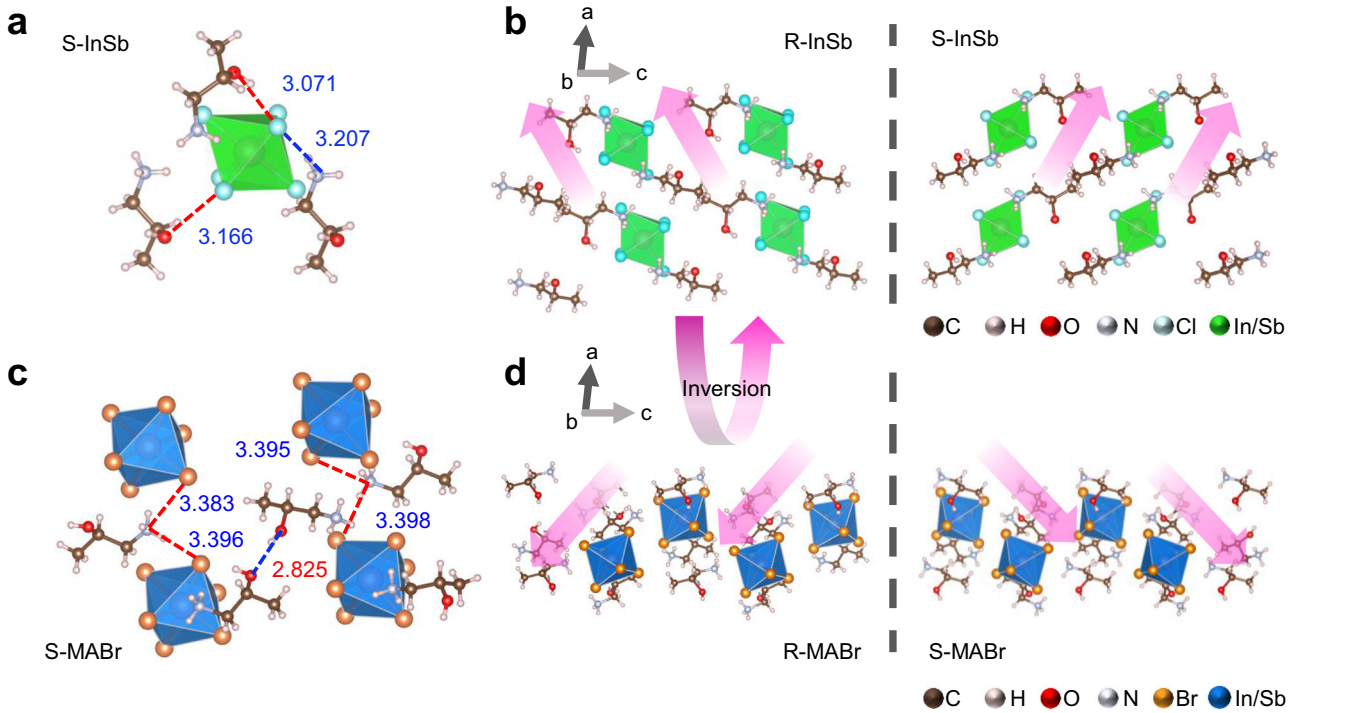

Fig. 4 | The single-crystal structure of R/S-InSb and R/S-MABr. a The hydrogen bonds distribution and bond length (Å) between chiral ligands and octahedron in S-InSb. **b** The single-crystal structure of R-InSb (left) and S-InSb (right), respectively. **c** The hydrogen bonds distribution and bond length (Å) between chiral ligands and octahedron in S-MABr. **d** The single-crystal structure of R-MABr (left) and S-MABr (right), respectively.

shows a negative signal CPL in the same region. The direction of the CPL signal is consistent with that of R/S-InSb (Fig. 3f). To further explore the near-infrared emission mechanism of R/S-FABr, the temperature-dependent PL spectra of S-FABr were acquired. Supplementary Fig. 30 reveals simultaneous thermal quenching and spectral broadening, the full width at half maximum (FWHM) increases from 165 to 194 nm as temperature rises from 260 to 340 K. This combination of phenomena aligns with characteristic signatures of self-trapped exciton (STE) emission. Quantitative analysis of electron-phonon coupling strength yields a Huang-Rhys factor $S = 30.25$, exceeding the strong-coupling threshold ($S > 5$). This confirms substantial electron-phonon interaction in the material. Meanwhile, the exciton binding energy extracted from Arrhenius fitting ($E_a = 138.50$ meV) ensures adequate stability of the self-trapped state at room temperature. It is noteworthy that the samples ground with MABr not only amplified the original CPL signal but also reversed the direction of the CPL signal. Among them, R-MABr shows a negative CPL signal, which is opposite to the CPL signal direction of R-InSb, and their enantiomers also show similar trends. Compared with the ground samples with inorganic salts (R/S-KBr and R/S-CsBr), the PLQY of the ground samples with organic salts (MABr, GuaBr and FABr) showed no improvement (Supplementary Table 8). Therefore, the grinding of organic salts for achieving chiral amplification may be related to the formation of more tightly bound hydrogen bonds with small-sized cations, which affects the chiral transfer process[52], which has been confirmed by Raman spectroscopy. Compared with the Raman spectra of S-InSb before grinding, the methylene stretching vibration band at 2915 cm^{-1} in S-MABr and S-GuaBr transformed from a single peak to a double peak after grinding (Supplementary Fig. 31). It indicates that the environment of the methylene group has changed due to the introduction of organic bromide salt. In the GuaBr grinding system, the characteristic sharp peak of pure GuaBr observed at 3317 cm^{-1} undergoes a distinct shift to a higher wavenumber region (3328 cm^{-1}) upon grinding, accompanied by noticeable peak broadening. This observation indicates that the Gua^+ cation plays a dual role in the post-grinding sample: it acts not only as a hydrogen bond donor but also contributes to the reconstruction and enhancement of the hydrogen bonding network (Supplementary Fig. 32). This resulted in an increase in the g_{lum} value of R/S-GuaBr, which was calculated as 1.34×10^{-2} and -1.45×10^{-2}, respectively. The 3289–3558 cm^{-1} region of S-MABr exhibited a broad envelope, indicative of dynamic reorganization in the hydrogen-bonding network. This structural reconfiguration is hypothesized to underpin the observed CPL signal inversion (Supplementary Fig. 33).

To elucidate the mechanism underlying CPL signal inversion, we obtained single-crystal structures of R/S-InSb and R/S-MABr via a slow-cooling crystallization method. Both compounds crystallize in the triclinic space group P1. In the crystal structure of S-InSb, the chiral structure is composed of In-Cl octahedra and chiral ligands. The chiral (R/S)-1-amino-2-propanol ligands were connected to the In^{3+} octahedra through three distinct hydrogen bonds. The hydroxyl group of the chiral ligand formed O-H···Cl hydrogen bonds with the Cl^- anion on the In^{3+} octahedron, with bond lengths ranging from 3.071 to 3.166 Å. The amino hydrogen formed longer N-H···Cl hydrogen bonds with the Cl^- anion on the octahedron (Fig. 4a and Supplementary Fig. 34). These hydrogen-bonding interactions collectively assemble into the crystal architecture depicted in Fig. 4b. Surprisingly, in the S-MABr crystal structure, we observed that methylamine molecules were not incorporated into the lattice. Instead, Br^- anions substituted for Cl^- anions on the In^{3+} octahedral after grinding. Notably, the hydrogen-bonding network in S-MABr exhibited greater complexity compared to S-InSb. In contrast to S-InSb where the chiral ligand exhibited three distinct hydrogen-bonding modes, (S)-(+)-1-amino-2-propanol in S-MABr exclusively forms N-H···Br hydrogen bonds with the octahedral Br^- anions, with bond lengths ranging from 3.383 to 3.398 Å (Fig. 4c and Supplementary Fig. 35). Additionally, a different O-H···O hydrogen bond (2.825 Å) emerged between two antiparallel chiral ligands. These hydrogen-bonding interactions collectively induce a more compact octahedral arrangement in S-MABr, enhancing CPL performance. Furthermore, by comparing the Raman spectra of S-MABr with those

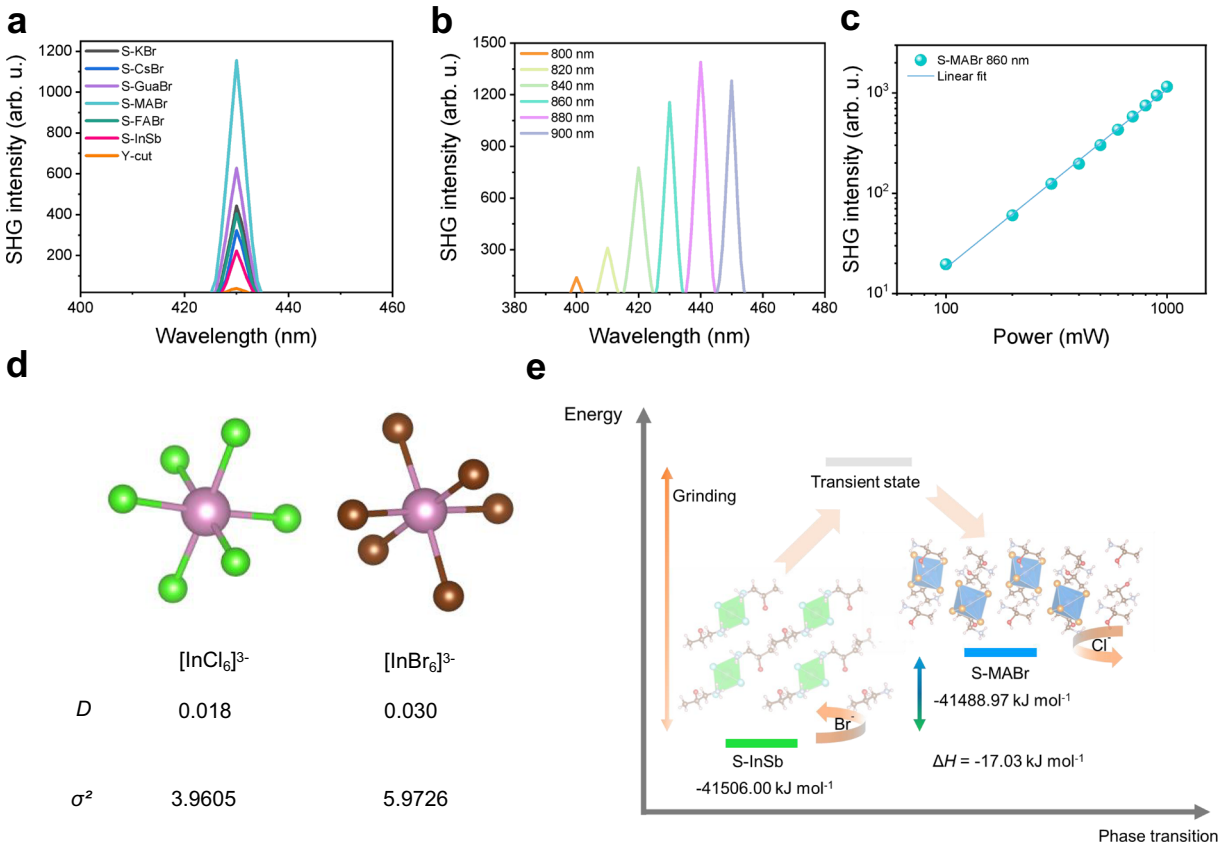

Fig. 5 | Nonlinear optical properties of grinding samples and the grinding mechanism. a The SHG Intensity of S-InSb, S-KBr, S-CsBr, S-GuaBr, S-MABr and S-FABr. **b** Wavelength-dependent SHG spectra of S-MABr excited from 800 to 900 nm laser. Laser power: 1 W. **c** Logarithmic plots of power-dependent SHG intensities, showing the quadratic relationship. Laser wavelength: 860 nm. The slope of ≈2 mW^{-1} in the linear fit of the logarithm plot indicates the second-order NLO. **d** the distortion degree of $[InCl_6]^{3-}$ and $[InBr_6]^{3-}$, *D*: off-centering distortion index), σ^2: bond angle variance, green: Cl, pink: In, brown: Br. **e** Schematic diagram illustrating the mechanism of transforming S-InSb into the S-MABr during the grinding process (The orange arrow represents that the grinding process promotes the phase transformation, The green, gray and blue colors respectively represent the energy levels of S-InSb, the transition state and S-MABr during the grinding process). Source data are provided as a Source data file.

of other ground samples, we discovered that the hydrogen bond form of S-MABr, which is consistent with the phenomenon mentioned earlier where the CPL signals of only R/S-MABr in the CPL spectrum reversed (Supplementary Fig. 36). Critically, the octahedral packing in S-MABr adopted a chiral arrangement opposite to that in S-InSb. This reversed octahedral organization post-grinding directly underpinned the observed CPL signal inversion. The newly formed hydrogen bonds during grinding play a pivotal role in driving the structural reversal.

Enhancement of SHG by grinding

The ground sample still exhibited symmetric CD signals, confirming non-centrosymmetry and SHG potential. To verify this hypothesis, we tested the SHG properties of the samples before and after grinding, excited by a 1 W 860 nm laser (Fig. 5a). The results demonstrated a universal enhancement in SHG intensity for all ground samples (KBr, CsBr, MABr, GuaBr, FABr) compared to the pristine S-InSb (Supplementary Table 9). Among them, S-MABr shows the most improvement, with an enhancement of 5.18 times compared to S-InSb and 29.71 times compared to the standard sample Y-cut quartz. These results further demonstrate the effectiveness of the grinding process in regulating the chiral optical properties. The nonlinear optics (NLO) properties of S-MABr were further studied. The SHG spectrum obtained under femtosecond laser excitation from 800 to 900 nm revealed efficient second-harmonic conversion (Fig. 5b). Moreover, the power-dependent SHG intensity curve shows that the SHG intensity increases quadratically with the input laser power (Supplementary Fig. 37). This quadratic increase in SHG intensity confirms the second-order nonlinear optical process (Fig. 5c)[53–55]. To elucidate the structural origin of the SHG enhancement, we quantified the distortion of the metal-halide octahedra in R/S-InSb and R/S-MABr (Fig. 5d). The off-centering distortion index (*D*) and bond angle variance (σ^2) are commonly used to quantify the asymmetry of the octahedra. The *D* and σ^2 are calculated using Eqs. (1) and (2) according to the refs. 56,57. The *D* index of $[InCl_6]^{3-}$ and $[InBr_6]^{3-}$ are 0.018 and 0.030, respectively. The σ^2 values of $[InCl_6]^{3-}$ and $[InBr_6]^{3-}$ are 3.9605 and 5.9726, respectively. This clear increase in both distortion parameters indicates that Br^- substitution induces greater octahedral distortion compared to Cl^-, which is the fundamental reason for the enhanced SHG response observed in S-MABr[58,59].

$$D = \sum_{i=1}^{3} \frac{|a_i - b_i|}{a_i + b_i} \quad (1)$$

$$\sigma^2 = \frac{1}{11} \sum_{i=1}^{12} (\theta_i - 90^\circ)^2 \quad (2)$$

Grinding mechanism

The crystalline architecture of R/S-InSb affords a distinctive capacity for mechano-responsive optical modulation via grinding. Firstly, the

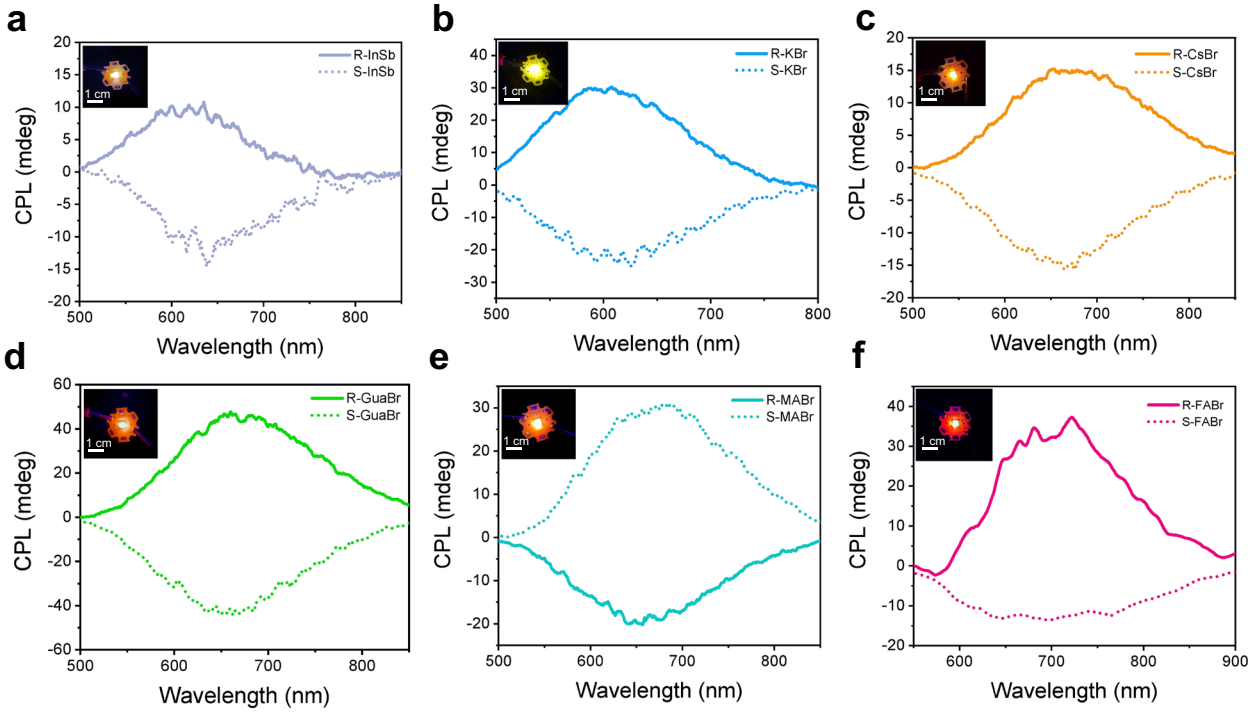

Fig. 6 | The applications of grinding strategy. The CPL spectra of CP-LED devices: (**a**) R/S-InSb, (**b**) R/S-KBr, (**c**) R/S-CsBr, (**d**) R/S-GuaBr, (**e**) R/S-MABr and (**f**) R/S-FABr. Source data are provided as a Source data file.

chiral ligand R/S-1-amino-2-propanol, classified as the alcohol amine category, contains hydroxyl groups. Due to the electronegativity of oxygen, the hydrogen on the hydroxyl group is more prone to dissociation compared to the hydrogen on the amino group in most of the amine ligands reported in ref. 60. This inherent characteristic facilitates the formation of dynamic hydrogen-bonding networks within the metal-halide framework, thereby promoting solid-state reactivity during grinding. Secondly, comparative analysis with reported InSb-based chiral metal halides reveals that the alkanolamine-ligated metal halide exhibits a lower octahedral distortion index[40]. This suggests that the hydrogen-bonding interactions between the chiral ligand and the $[InCl_6]^{3-}$ octahedra are comparatively weaker than those in structures ligated by aliphatic or aromatic amines. Such structural characteristics provide a mechanistic basis for the occurrence of grinding-induced solid-state reactions.

Substantial structural reorganization is corroborated by unit cell parameter analysis. The parameters for S-InSb ($\alpha = 84.790°$, $\beta = 84.016°$, $\gamma = 64.131°$) shift upon grinding with MABr, yielding S-MABr with parameters $\alpha = 68.381°$, $\beta = 75.213°$, $\gamma = 71.843°$. This pronounced change unequivocally indicates a major crystal phase transition. To gain deeper insight into the grinding-induced reaction, we performed density functional theory (DFT) calculations to simulate the interaction between S-InSb and MABr. The computed reaction enthalpy is $\Delta H = -17.03\ kJ\ mol^{-1}$ (Fig. 5e), suggesting an exothermic process. It is thus plausible that a fraction of the mechanical energy input during grinding is converted into localized heat, elevating the temperature at the interface and driving the chemical transformation. Consequently, the crystal undergoes a phase transition from S-InSb to S-MABr, a process that entails reversal of the octahedral arrangement direction, adoption of a more compact structural packing, and halogen substitution.

Application in CP-LEDs

Owing to the grinding strategy that confers samples with wavelength-tunable luminescence performance and CPL characteristics, the samples were pasted on a commercial GaN ultraviolet light-emitting diode (UV-LED) chip (365 nm, 1.0 W) to get the CP-LED device at the 5 V driving voltage, the CPL properties of the UV-LED devices were characterized (Fig. 6a–f). It is worth noting that a series of CP-LED devices exhibit mirror-symmetric CPL signals within the range of 500–900 nm, with the position of the main emission peak wavelength and the circularly polarized direction being highly consistent with the previously measured CPL spectra. Notably, the CP-LED devices fabricated with the R-GuaBr and S-GuaBr samples exhibited the maximum $|g_{lum}|$ values of $\approx +1.37 \times 10^{-2}$ and -1.98×10^{-2}, respectively (Supplementary Fig. 38). This indicates that the materials obtained through the grinding strategy have great application potential for CP-LED devices.

Discussion

In summary, we synthesized a phosphorescent indium-based chiral metal halide (R/S-In) using (R/S)-1-amino-2-propanol as the chiral ligand. R-In and S-In not only have a phosphorescence lifetime of up to 96.74 and 86.34 ms, respectively, but also exhibits blue CPL emission characteristics. Subsequent doping with Sb^{3+} ions afforded R/S-InSb, which show a distinct red-shifted orange CPL emission. Based on R/S-InSb, we developed a post-regulation strategy for chiral optical properties, utilizing the mechanical force of grinding to generate energy to form a modified structure for boosting the chiral optical properties of the metal halide. This strategy demonstrates certain universality. After grinding with inorganic salts, R/S-InSb amplifies the CPL signal to the 10^{-2} level. By grinding with organic salts, the non-chiral amine hydrogen bond could enhance the chiral induction effect, increasing the CPL signal by one order of magnitude. Interestingly, by rational selection of cations, the direction of the CPL signal could be reversed. Furthermore, employing FABr for grinding generated a NIR CPL emission with a substantial Stokes shift of 370 nm, accomplished without incorporating rare-earth metals or iodide ions. The grinding post-regulation strategy provides an approach for the post-regulation of CPL materials, facilitating the convenient and efficient adjustment of the signal intensity, direction, and emission position of CPL. The nonlinear optical properties can also be amplified using this strategy, where S-MABr shows the most improvement, with an enhancement of 5.18

times compared to S-InSb, and 29.71 times that of the standard sample Y-cut quartz. Meanwhile, the grinding strategy endows the material with flexible and adjustable chiral optical properties, making it have great application prospects in the field of CP-LEDs. The post-regulation strategy for the flexible regulation of the chiral optical properties of metal halides, laying the foundation for their application in optical and other fields.

Methods

Materials

Indium(III) chloride ($InCl_3$), (R)-1-amino-2-propanol, (S)-1-amino-2-propanol, *N,N*-dimethylformamide (DMF) were purchased from Heowns. Antimony trichloride ($SbCl_3$) was purchased from Meryer. Potassium bromide (KBr), cesium bromide (CsBr), methylamine bromide (MABr), guanidinium bromide (GuaBr), and formamidine bromide (FABr) was purchased from Macklin. Hydrochloric acid (36–38%) was purchased from Tianjin Fengchuan chemical company.

Synthesis of R-/S-1-amino-2-propanol hydrochloride. R-/S-1-amino-2-propanol (0.05 mol) was added to absolute ethanol (20 mL) and dissolved into a pellucid yellow transparent solution under stirring at room temperature. Then, hydrochloric acid (36–38%, 10 mL) was dripped into the reaction system with a dropping funnel at a uniform speed, and the reaction continued for 4 h until white powder was gradually precipitated. After the reaction, absolute ether was added for washing, filtering and repeating three times to obtain white powder. Finally, the product was dried in a vacuum drying oven at 50 °C for 6 h to obtain R-/S-1-amino-2-propanol hydrochloride.

Synthesis of R/S-In crystals. $InCl_3$ (1 mmol, 221.4 mg) and R-/S-1-amino-2-propanol hydrochloride (2 mmol, 222.2 mg) was added to hydrochloric acid (36–38%, 2 mL) to react at 90 °C until the solid was completely dissolved, and the reaction continued for 2 h. After the reaction, the reaction solution was naturally cooled to room temperature, resulting in crystals to grow. Finally, R/S-In crystals were obtained by filtering, washing and drying.

Synthesis of Sb^{3+}-doped R/S-InSb single crystals. 15% of $InCl_3$ in the precursor is replaced by $SbCl_3$, and the total molar amount remains unchanged. The synthesis of R/S-InSb single crystals is as follows. $InCl_3$ (0.85 mmol, 187.2 mg), $SbCl_3$ (0.15 mmol, 34.8 mg) and R-/S-1-amino-2-propanol hydrochloride (2 mmol, 222.2 mg) was added to hydrochloric acid (36–38%, 2 mL) to react at 90 °C until the solid was completely dissolved, and the reaction continued for 2 h. Subsequent steps remain the same with that of R/S-In. Finally, R/S-InSb single crystals were obtained by filtering, washing and drying.

Synthesis of Sb^{3+}-doped R/S-MABr single crystals. The synthesis of R/S-MABr single crystals is as follows. $InCl_3$ (0.85 mmol, 187.2 mg), $SbCl_3$ (0.15 mmol, 34.8 mg), R-/S-1-amino-2-propanol hydrochloride (2 mmol, 222.2 mg) and methylammonium bromide (2 mmol, 223.94 mg) was added to hydrochloric acid (36–38%, 2 mL) to react at 90 °C until the solid was completely dissolved, and the reaction continued for 2 h. Subsequent steps remain the same with that of R/S-In. Finally, R/S-InSb single crystals were obtained by filtering, washing and drying.

Sample preparation for CPL/CD measurements. The powder was dissolved anhydrous DMF under mild stirring to form a clear, homogeneous solution. The solution was then spin-coated onto meticulously cleaned quartz substrates. The spin-coating parameters were rigorously controlled: a speed of 2000 revolutions per minute (rpm) for a duration of 30 s. Immediately after spin-coating, the films were transferred to a hotplate and annealed at 100 °C for 10 min.

Characterization

A LAMBDA 750 ultraviolet spectrometer was used to measure the UV-visible absorption spectrum of solids. PL spectrum, PLE spectrum, delayed PL spectrum and PLQY were measured at Edinburgh FLS1000 under excitation at 365 nm.

Single crystals of R/S-InSb were recorded using the Bruker D8 Venture TXS PHOTON 100 diffractometer. The crystal was kept at 100 K during data collection. Using Olex2, the structure was solved with the SHELXT structure solution program using Intrinsic Phasing and refined with the SHELXL refinement package using Least Squares minimization.

The crystal structure of chiral In-based metal halide powders has been characterized by an X-ray diffractometer with Cu K_α radiation (λ = 1.5418 Å). The measurement range is 5–90° and the scanning speed is 10° min^{-1}.

The X-ray photoelectron spectroscopy (XPS) measurements were performed with a Thermo Fisher Scientific ESCALAB 250Xi spectrometer using a monochromatic Al K_α source (1486.6 eV). All spectra were charge-corrected to the C 1*s* peak at 284.8 eV.

TEM images and elemental distributions of the samples were collected on a field-emission transmission electron microscope JEM-F200.

The CD spectra was tested at room temperature with JASCO-J1700 CD spectrometer (scan speed 500 nm min^{-1} (digital integration time (DIT): 1 s).

CPL was tested with the circularly polarized PL spectrometer of CPL-300 (scan speed 500 nm min^{-1}, DIT: 1 s).

The SHG spectra was measured with a WITec alpha300R.

The LED device is made by mixing grinding samples with PDMS and then coating it on the commercialized UV-LED chips. Excitation is carried out with the current of 5 V 0.2 A.

All the calculations are implemented by the VASP code. The GGA-PBE functional is selected for the exchange and correlation potential. Weak van der Waals interaction is considered by the DFT-D3 functional. The cut-off energy for the plane-wave is 400 eV. The Gamma point in the Brillouin-zone is chosen for integration. Total energies of the systems converge to 10^{-5} eV in the iteration solution of Kohn-Sham equation. The force on each atom reduces to 0.05 eV $Å^{-1}$ after geometry optimization.

Reporting summary

Further information on research design is available in the Nature Portfolio Reporting Summary linked to this article.

Data availability

The data that support the findings of this study are available from the corresponding authors upon request. X-ray crystallographic structures have been deposited at the Cambridge Crystallographic Data Center (CCDC), under deposition numbers: 2482886 (R-InSb), 2482887 (R-MA), 2482888 (S-InSb) and 2482889 (S-MA). Source data are provided with this paper.

References

1. Liu, Y., Wei, Y. & Quan, Z. Regulating circularly polarized luminescence in zero-dimensional chiral hybrid metal halides. *Acc. Mater. Res.* **6**, 638–647 (2025).
2. Dong, Y. et al. Chiral perovskites: promising materials toward next-generation optoelectronics. *Small* **15**, 1902237 (2019).
3. Ji, M.-J., Zhao, W.-L., Li, M. & Chen, C.-F. Circularly polarized luminescence with high dissymmetry factors for achiral organic molecules in solutions. *Nat. Commun.* **16**, 2940 (2025).
4. Li, M., Li, M., Liu, X., Yuan, Y. & Zhao, G. Domain-confined perovskite in lanthanide MOFs for multiresponse CPL switches and information encryption. *ACS Appl. Mater. Interfaces* **17**, 36899–36911 (2025).

5. Zhao, T. & Duan, P. Photon upconversion cooperates with downshifting in chiral systems: modulation, amplification, and applications of circularly polarized luminescence. *Angew. Chem., Int. Ed.* **63**, e202406524 (2024).
6. Xu, M. et al. Mechanically responsive circularly polarized luminescence from cellulose-nanocrystal-based shape-memory polymers. *Adv. Mater.* **35**, 2301060 (2023).
7. Guo, Z., Li, J., Chen, R. & He, T. Advances in single crystals and thin films of Chiral Hybrid Metal Halides. *Prog. Quantum Electron.* **82**, 100375 (2022).
8. Cheng, Q., Hao, A. & Xing, P. A chemosensor-based chiral coassembly with switchable circularly polarized luminescence. *Nat. Commun.* **12**, 6320 (2021).
9. Kumar, V. et al. Chiral nanographenes exhibiting circularly polarized luminescence. *Chem. Soc. Rev.* **54**, 4922–4947 (2025).
10. Han, D. et al. Endowing inorganic nanomaterials with circularly polarized luminescence. *Aggregate* **3**, e148 (2022).
11. Lin, S. et al. Photo-triggered full-color circularly polarized luminescence based on photonic capsules for multilevel information encryption. *Nat. Commun.* **14**, 3005 (2023).
12. Zor, E., Bingol, H. & Ersoz, M. Chiral sensors. *TrAC. Trends Anal. Chem.* **121**, 115662 (2019).
13. Zhang, R. et al. Energy transfer for constructing circularly polarized luminescence materials: recent progress and future prospects. *Adv. Funct. Mater.* **35**, 2417308 (2025).
14. Kitzmann, W. R., Freudenthal, J., Reponen, A.-P. M., VanOrman, Z. A. & Feldmann, S. Fundamentals, advances, and artifacts in circularly polarized luminescence (CPL) spectroscopy. *Adv. Mater.* **35**, 2302279 (2023).
15. Zhai, L. et al. Efficient circularly polarized luminescence from Mn–Br hybrid perovskite assembled by achiral architectures. *Angew. Chem., Int. Ed.* **64**, e202425543 (2025).
16. Zhang, C., Li, S., Dong, X.-Y. & Zang, S.-Q. Circularly polarized luminescence of agglomerate emitters. *Aggregate* **2**, e48 (2021).
17. Li, Y. et al. Design strategies and emerging applications of perovskite-based sensors. *SmartMat* **6**, e70022 (2025).
18. Peng, Q.-C. et al. High performance dynamic X-ray flexible imaging realized using a copper iodide cluster-based MOF microcrystal scintillator. *Angew. Chem., Int. Ed.* **62**, e202308194 (2023).
19. Liu, D.-Y. et al. Reversible local protonation-deprotonation: tuning stimuli-responsive circularly polarized luminescence in chiral hybrid zinc halides for anti-counterfeiting and encryption. *Angew. Chem., Int. Ed.* **63**, e202410416 (2024).
20. Wang, S., Zhang, Y., Halasyamani, P. S. & Mitzi, D. B. Chirality and solvent coassist the structural evolution of hybrid manganese chlorides with second-harmonic-generation response. *Inorg. Chem.* **63**, 16121–16127 (2024).
21. Yao, J. et al. Efficient spin-light-emitting diodes with tunable red to near-infrared emission at room temperature. *Adv. Mater.* **37**, 2413669 (2025).
22. Liu, Y. et al. Near-infrared light emitting metal halides: materials, mechanisms, and applications. *Adv. Mater.* **36**, 2312482 (2024).
23. Song, Z. et al. Methanol-induced crystallization of chiral hybrid manganese (II) chloride single crystals for achieving circularly polarized luminescence and second harmonic generation. *Adv. Opt. Mater.* **12**, 2301272 (2024).
24. Chen, J. et al. Structural origin of enhanced circularly polarized luminescence in hybrid manganese bromides. *Angew. Chem., Int. Ed.* **61**, e202205906 (2022).
25. Tao, M., Cao, R., Sun, S., Li, H. & Xiao, Y. Chiral zero-dimensional hybrid antimony chloride with circularly polarized luminescence and solvent-induced property regulation. *Chem. - Eur. J.* **31**, e202404470 (2025).
26. Liu, D.-Y., Li, H.-Y., Han, R.-P., Liu, H.-L. & Zang, S.-Q. Multiple stimuli-responsive luminescent chiral hybrid antimony chlorides for anti-counterfeiting and encryption applications. *Angew. Chem., Int. Ed.* **62**, e202307875 (2023).
27. Sun, M.-E. et al. Pressure-driven circularly polarized luminescence enhancement and chirality amplification. *J. Am. Chem. Soc.* **147**, 10706–10714 (2025).
28. Sun, M.-E. et al. Chirality-dependent structural transformation in chiral 2D perovskites under high pressure. *J. Am. Chem. Soc.* **145**, 8908–8916 (2023).
29. Sui, L. et al. Breaking mirror circularly polarized luminescence of chiral metal–organic frameworks by high-pressure stimulation. *CCS Chem* **5**, 2215–2224 (2023).
30. Chen, G. et al. Nucleation-mediated growth of chiral 3D organic–inorganic perovskite single crystals. *Nat. Chem.* **15**, 1581–1590 (2023).
31. Dang, Y., Liu, X., Cao, B. & Tao, X. Chiral halide perovskite crystals for optoelectronic applications. *Matter* **4**, 794–820 (2021).
32. Yamanoi, Y. Hydrosilane/organoiodine coupling-enabled studies of organosilane physical properties. *Acc. Chem. Res.* **56**, 3325–3341 (2023).
33. Ma, X.-H. et al. High-efficiency pure blue circularly polarized phosphorescence from chiral N-heterocyclic-carbene-stabilized copper(I) clusters. *J. Am. Chem. Soc.* **145**, 25874–25886 (2023).
34. Nie, X. et al. Dynamic chirality in nature-inspired photonic crystal films: ultralong room temperature phosphorescence and stimuli-responsive circularly polarized luminescence. *ACS Nano* **19**, 11221–11229 (2025).
35. Chen, X. et al. Dual-emission mechanism for tunable white light emission from an economical OIHMH crystal of $(TEA)_2ZnCl_4:Sb^{3+}$. *Chem. Eng. J.* **505**, 159720 (2025).
36. Wu, J. et al. Ultrafast study of exciton transfer in Sb(III)-doped two-dimensional $[NH_3(CH_2)_4NH_3]CdBr_4$ perovskite. *ACS Nano* **15**, 15354–15361 (2021).
37. Pinchetti, V. et al. Magnetic transitions and energy transfer processes in Sb-based zero-dimensional metal halide nanocrystals doped with manganese. *ACS Energy Lett.* **7**, 1566–1573 (2022).
38. Bai, T. et al. From dopant to host: solution synthesis and light-emitting applications of organic-inorganic lanthanide-based metal halides. *Small Struct* **5**, 2400096 (2024).
39. Yang, Z. et al. A universal strategy to enhance circularly polarized luminescence brightness in chiral perovskites. *Laser Photonics Rev.* **18**, 2400040 (2024).
40. Wang, Z. et al. Turn-on circularly polarized luminescence in chiral indium chlorides by 5s2 metal centers. *Angew. Chem., Int. Ed.* **62**, e202215206 (2023).
41. Deng, Y. et al. Chiral induction and Sb^{3+} doping in indium halides to trigger second harmonic generation and circularly polarized luminescence. *Chin. Chem. Lett.* **35**, 109085 (2024).
42. Shi, C.-M. et al. Stepwise amplification of circularly polarized luminescence in indium-based metal halides by regulating their structural dimension. *Nat. Commun.* **16**, 1505 (2025).
43. Du, L. et al. Efficient circularly polarized luminescence and bright white emission from hybrid indium-based perovskites via achiral building blocks. *Adv. Funct. Mater.* **34**, 2315676 (2024).
44. Liu, X. et al. A-site coordinating cation engineering in zero-dimensional antimony halide perovskites for strong self-trapped exciton emission. *SmartMat* **5**, e1224 (2024).
45. Hu, M. et al. Tunable circularly polarized luminescence from single crystal and powder of the simplest tetraphenylethylene helicate. *ACS Nano* **15**, 16673–16682 (2021).
46. Christou, C., Agapiou, A. & Kokkinofta, R. Use of FTIR spectroscopy and chemometrics for the classification of carobs origin. *J. Adv. Res.* **10**, 1–8 (2018).
47. Niu, X. et al. Chiral europium halides with high-performance magnetic field tunable red circularly polarized luminescence at room temperature. *Nat. Commun.* **16**, 2525 (2025).

48. Wang, Z. et al. Against the Wallach's rule through rational design of metal-free chiral perovskites toward efficient red circularly polarized phosphorescence. *Angew. Chem., Int. Ed.* **64**, e202501360 (2025).
49. Debnath, G. H., Mukherjee, P. & Waldeck, D. H. Identifying lanthanide energy levels in semiconductor nanoparticles enables tailored multicolor emission through rational dopant combinations. *Acc. Chem. Res.* **58**, 1473–1483 (2025).
50. Yang, Y.-N. et al. Pressure-activated efficient near-infrared luminescence in atomically precise gold nanoclusters. *J. Am. Chem. Soc.* **147**, 26991–26999 (2025).
51. Feng, H. et al. An alloy engineering strategy toward helical microstructures of achiral π-conjugated molecules for circularly polarized luminescence. *J. Am. Chem. Soc.* **147**, 9250–9260 (2025).
52. Li, J. et al. Regulating second-harmonic generation in 2d chiral perovskites through achiral organic spacer cation alloying strategy. *Laser Photonics Rev.* **19**, 2401379 (2025).
53. Han, X. et al. Linear optical afterglow and nonlinear optical harmonic generation from chiral tin(iv) halides: the role of lattice distortions. *Mater. Horiz.* **10**, 1005–1011 (2023).
54. Zheng, Y. et al. Induction of chiral hybrid metal halides from achiral building blocks. *J. Am. Chem. Soc.* **144**, 16471–16479 (2022).
55. Zhao, Y. et al. Reversible phase transition for switchable second harmonic generation in 2D perovskite microwires. *SmartMat* **3**, 657–667 (2022).
56. Guan, J. et al. Inverted chiroptical properties of hybrid metal halides through reversible chiral induction driven by external and internal chirality transfer. *Angew. Chem., Int. Ed.* **64**, e202503083 (2025).
57. Nam, S. H. et al. Structural asymmetry and chiral-induced spin selectivity in chiral palladium-halide semiconductors. *J. Am. Chem. Soc.* **146**, 15045–15052 (2024).
58. Qu, J. et al. Origin of pressure-induced nonlinear optical property enhancement in $CsGeCl_3$ perovskite: $[GeCl_6]$ octahedron distortion and band gap closing. *J. Am. Chem. Soc.* **147**, 6717–6726 (2025).
59. Guan, J. et al. Free halogen substitution of chiral hybrid metal halides for activating the linear and nonlinear chiroptical properties. *J. Am. Chem. Soc.* **145**, 26833–26842 (2023).
60. Mullay, J. Atomic and group electronegativities. *J. Am. Chem. Soc.* **106**, 5842–5847 (1984).

Acknowledgements

We are grateful to the National Natural Science Foundation of China (22278315).

Author contributions

J.H.W.: Conceptualization, investigation, formal analysis, writing-original draft, writing—review & editing. H.L.: Conceptualization, investigation. J.L.W.: Methodology, formal analysis. X.Y.: Data curation, formal analysis. T.Z.: Methodology, writing—review & editing. B.L.: Methodology, writing—review & editing. S.J.: Supervision, project administration, writing—review & editing.

Competing interests

The authors declare no competing interests.

Additional information

Supplementary information The online version contains supplementary material available at https://doi.org/10.1038/s41467-026-69353-9.

Correspondence and requests for materials should be addressed to Shuang Jiang.

Peer review information *Nature Communications* thanks Young-Hoon Kim, and the other, anonymous, reviewer(s) for their contribution to the peer review of this work. A peer review file is available.